Intergranular corrosion in evolving media: Experiment and modeling by cellular automata

S. Guiso, N. Brijou-Mokrani, J. de Lamare, Dung Di Caprio, B. Gwinner, V. Lorentz, F. Miserque

Is there a memory effect of intergranular corrosion?

S. Guiso[a], N. Brijou-Mokrani[a], J. de Lamare[a], D. Di Caprio[b], B. Gwinner[a], V. Lorentz[a] and, F. Miserque[a],

[a] Université Paris-Saclay, CEA, Service de la Corrosion et du Comportement des Matériaux dans leur Environnement, 91191, Gif-sur-Yvette, France

[b] Chimie ParisTech, PSL Research University, CNRS, Institut de Recherche de Chimie Paris (IRCP), F-75005 Paris, France

Abstract

In this paper, we investigated the impact of the oxidizing character of the nitric medium on the evolution of the intergranular corrosion of a 310L austenitic stainless steel. Corroded surfaces were investigated by X-ray photoelectron spectroscopy. Optical observations were made to characterize the dimensions of the grooves on samples cross sections. Modeling and numerical simulations were carried out by using the cellular automata method. In two different stationary oxidizing conditions ("severe" in presence of oxidizing ions and "soft" without, respectively), we showed that the corroded surface of the steel reaches a different steady state: the oxide is thicker, the intergranular grooves are thinner and the surface area is larger with the oxidizing character of the nitric medium. Then we investigated the effect of an alternative "severe then soft" corrosion sequence. We showed that the system re-adapted to the soft conditions without memory effect from the previous severe ones.

Keywords

Austenitic stainless steel, Cellular automata modeling, Intergranular corrosion, Nitric acid, XPS

Introduction

Grains boundaries in materials are often considered as a weakness regarding the chemical attack by the environment. The preferential attack of these grains boundaries results in a specific corrosion mode named intergranular corrosion (IGC). Challenges relative to intergranular corrosion concern various materials such as nickel based alloys [1-3], aluminum based alloys [4-6] or steels [7-9]. One specific issue is about IGC of non-sensitized stainless steels (SSs) in nitric acid. This is mainly linked to the domain of the spent nuclear fuel reprocessing, where SSs are used for containing nitric acid solutions at

various concentrations and temperatures [10-12]. IGC of non-sensitized SSs is induced by a differential of reactivity between grains and grains boundaries. Therefore, grain boundaries are preferentially dissolved compared to the grains themselves. Consequently, grooves are formed along the grains boundaries, which progression in the SS generates a periodic detachment of grains.

Over the last fifteen years, IGC of non-sensitized SSs has been investigated through both experimental and modeling approaches. From the experimental point of view, different techniques are used to characterize IGC. In addition to qualitative observations of the surface, optical or scanning electron microscopy can be performed on the cross section of the sample to geometrically characterize the intergranular grooves in 2D [13-23]. A promising 3D characterization approach has also been attempted by µ-Xray-tomography [24]. The measurement of the mass loss as the function of time gives also important information regarding the kinetics of IGC [13, 15, 19-21, 25-32]. Sometimes, the chemical characteristics of the surface are analyzed by X-ray photoelectron spectroscopy (XPS) [15, 28, 33, 34]. An attempt to characterize IGC with ultrasonic methods was proposed by Jothilakshmi *et al.* [22]. In addition to this experimental information, different models were recently proposed to simulate IGC of non-sensitized SSs in nitric acid. A simple analytical approach was proposed for simulating the evolution of the mass loss [35]. A geometrical approach in 2D was developed for simulating the evolution of the interface of the material suffering IGC [21, 35]. More realistic models were also developed using the method of cellular automata (CA) for simulating the geometrical evolution of the material in a 3D realistic granular structure [18, 32, 36-38].

All these experimental and modeling approaches allowed studying the influence of different metallurgical and chemical parameters on IGC. It appears that IGC could be dependent on the surface exposed to corrosive medium regarding the rolling direction [19, 20, 29, 39], on the chemical composition of the SSs, which in turn influence the chemical composition of the grains boundaries [13, 14, 18, 20, 28, 31, 33, 34, 40, 41], on the grains size [30] and on the metallurgical treatment [25]. IGC of SSs was also studied in a pure nitric medium at different concentrations [28, 33] but also with the addition of different oxidizing species at different levels [26, 27, 39, 41]. However, these parameters were only correlated to the corrosion potential and corrosion kinetics, with no information on the characteristics of the interface in terms of chemical composition and morphology. In this paper, we intend to fill this gap by investigating IGC of a SS in two different nitric acid

media. We investigated the influence of the chemical medium nature on the elemental composition of the oxide layer (analyzed by XPS) and the geometrical characteristics of the interface. For this last one, as it was difficult to extract information from experiments, we used CA modeling. Indeed, we showed that CA is able to reproduce accurately the experimental behavior [23, 38].

Moreover, we also investigated cases where the corrosive environment evolves over time during a given experiment. The objective was to study how the IGC of a given SS sample may be influenced by the fact that this SS was previously corroded in a first medium. To our knowledge, this aspect has never been studied despite it may concern many industrial issues, for example: the case of equipments whose corrosive environment evolves with time or the case of the alternation of phases of rinsing (with one first chemical medium) and working (in a second chemical medium).

Experimental and modeling approaches

Experimental conditions and characterization methods

We performed corrosion tests (electrochemical measurements and immersion tests) with an AISI 310L SS provided by Creusot Loire Industrie. This stainless steel has a low carbon content and was annealed and quenched. The chemical composition is given in Table 1. The mean grain size (84 µm) was determined using the normalized NF EN ISO 643:2003.

Table 1. Chemical Composition of AISI 310L SS (in wt.%).

Fe	C	Cr	Ni	Mn	Si	P	S	Mo	Nb
bal.	0.006	24.32	21.13	1.03	0.13	0.016	0.001	0.08	0.115

For the corrosion tests, the corrosion medium was 8 $mol.l^{-1}$ nitric acid at boiling point temperature (111 °C) containing or not 150/300 mg/L of vanadium(V) (introduced as 268/536 mg/L of V_2O_5). By introducing or not vanadium(V), we intended to impose different oxidizing conditions to the material regarding the difference of standard potential in nitric acid ($E°(NO_3^-/HNO_2)$ = 0.934 mV/SHE at 25 °C [42]) and in presence of vanadium(V), ($E°(VO_2^+/VO^{2+})$ = 1.004 V/SHE at 25 °C [42]). For the rest of the paper, we name “soft” conditions” the experiments without vanadium(V) and “severe conditions” the ones with additions of vanadium(V).

We performed electrochemical measurements (open circuit potential and linear voltammetry measurements) using a classical 3-electrodes configuration. The working and the counter electrodes were a 310L bullet shaped electrode (surface area 2 mm^2) and a platinum basket, respectively. The reference electrode was a mercury/mercurous sulfate electrode (Hg/Hg_2SO_4 - MSE, E = +0.65 V/SHE at 25 °C). The electrochemical measurements were performed using a VSP workstation controlled by the software EC-Lab v.10.37 (Biologic).

The conditions and durations of the 3 immersion tests are given in Table 2. SS specimens were 30 × 20 × 1.5 mm^3 parallelepiped samples. They were ultrasonic degreased with an ethanol/acetone mixture. They were pickled with an $H_2O/HCl/HNO_3/HF$ mixture for around 15 minutes in order to dissolve a thickness of about 20 µm. The experimental device consists of a 1 L glass reactor where 3 specimens are suspended to test the reproducibility of the corrosion process (the metallic surface area on the solution volume S/V ratio was 0.4 dm^2/L). The specimens were periodically removed from the reactor, rinsed with demineralized water and ethanol, dried with compressed air and weighted (AT 20 balance model from Mettler-Toledo, precision 0.01 mg). The solution was renewed after each corrosion period. The mass loss as a function of time was expressed in terms of equivalent thickness loss assuming a hypothetical homogeneous corrosion, as follows:

$$\Delta e = \Delta m / (\rho \times S) \times 10^4 \qquad \text{Equation 1}$$

With Δe the equivalent thickness loss (in µm)

Δm the measured mean mass loss (in g)

ρ the SS density (8 g/cm^3 approx.).

S the sample surface (13.5 cm^2)

Periodically, one of the samples was cut and thecross-section of the sample was optically observed (GX51 microscope model from Olympus).

Table 2: Conditions of the immersion corrosion tests. In tests n°1 and n°2, the corrosive medium remained constant during the test. In test n°3, the corrosive medium was modified after 1935 h.

Test		Conditions	Duration
Test n°1		Severe	t_{severe} = 2564 h
Test n°2		Soft	t_{soft} = 16815 h
Test n°3	Phase n°1	Severe	t_{severe} = 1935 h
	Phase n°2	Soft	t_{soft} = 16815 h (t_{test3} = $t_{severe+soft}$ = 17783 h)

XPS analyses were carried out with a Thermofisher Escalab 250 XI spectrometer using a monochromatic X-ray Al Ka source. The instrument was calibrated in energy with the Ag Fermi level (0 eV) and the $3d_{5/2}$ core level of metallic silver (368.3 eV). The C-1s signal was used to correct a possible charge effect: the CC/CH contribution of C-1s spectra was fixed at 285.0 eV. The analysis zone consisted of a 900 µm diameter spot. The data processing was performed using the commercially available Avantage^{TM} software. For the fitting procedure, a Shirley background has been used and Lorentzian-Gaussian (L/G) ratio was fixed at 30%. For the determination of relative proportions of oxide and metallic contribution, Ni-$2p_{3/2}$, Cr-$2p_{3/2}$ and Fe-$2p_{3/2}$ spectra have been deconvoluted. The main contributions used are presented in Table 3. Several arbitrary contributions are necessary to fit the iron and chromium oxide due to a multiplet splitting making the spectral analysis particularly complex [43, 44]. Nickel element is observed only metallic chemical state.

Table 3: Parameters used for the deconvolution of Cr, Ni and Fe-$2p_{3/2}$ core level spectra (Avantage^{TM} software) binding energies and full width at half maximum (FWHM).

	Ni-$2p_{3/2}$	**Fe-$2p_{3/2}$**			**Cr-$2p_{3/2}$**			
Chemical state	Metallic	Metallic	Oxide		Metallic	Oxide		
			Peak 1	Peak 2		Peak 1	Peak 2	Peak 3
Binding Energy (eV)	853.0 ± 0.3	853.0 ± 0.3	709.8 ± 0.3	712.0 ± 0.3	853.0 ± 0.3	576.1 ± 0.3	577.3 ± 0.3	578.5 ± 0.3
FWHM (eV)	1.4	1.0	3.0	3.3	1.5	1.7	1.8	1.9

Cellular Automata model

CA approach consists first in discretizing a volume (box) into a 3D hexagonal grid of cells. In our model ([23]), a cell can belong to a grain (GRN state), a grain boundary (IGN state) or the solution (SOL state). The material granular microstructure is obtained numerically by a Voronoi diagram (Figure 1). Furthermore, the SOL state is assigned to the three uppermost xy-layers: during dissolution, the solution path is conducted from the top of the grid to the bottom.

The kinetics of the reactions are hereby converted into corrosion probabilities, which drive the step from a time t to the following $t + \Delta t$. Given CA cells interact with their neighbouring ones according to their states, following transition rules. IGN and GRN cells change their states to SOL (this switch indicates that the IGN or GRN cell is corroded) according to two probabilities (input data fixed by the user), P_{ign} for grain boundaries and P_{grn} for grains. The way to fix the values of P_{ign} and P_{grn} so as to reproduce adequately the experimental results (with CA to experiments conversion factors) is described in reference [23].

The code has been written in C language, in CUDA environment, and numerical simulations have been performed using NVIDIA Tesla K80 in Dell PowerEdge C4130 servers with Intel Xeon E5-2640 processors. In the case of a (XYZ dimensions) 3D grid, a simulation run for a single experiment takes from one to a few days, depending on the values that are given to P_{grn} and P_{ign} (the higher the values, the lower the simulation time). The grids taken for the simulation are boxes of 1280x1280x1280 cells, and the number of

Voronoï structures are one hundred. This corresponds to a surface dimension of 13.5 mm^2 and a depth of 395 µm, using the scale transformation of 0.309 µm/cell as described in [23]. The results are averaged over the hundred different Voronoï structures and the errors bars given further in the paper represent their dispersion.

From the corroded sample at a time t, we can estimate the mass loss and the mean groove angle α' ([23]), as well as the relative surface in contact with the corrosive medium (see appendix 1 and 2). Note that the notation α' refers to the angle determined in 2D from virtual cross-sections of the 3D grid and that its distribution is slightly different from the 3D angles α distribution as discussed in [23, 24].

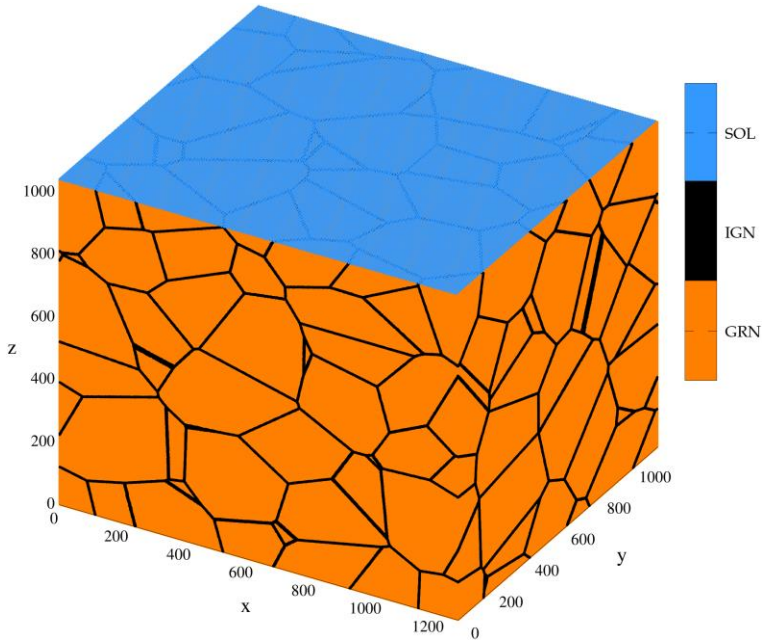

Figure 1: Representation of a 3D initial grid considered for the IGC model obtained numerically by a Voronoï diagram (GRN state cell in orange, IGN state cell in black and SOL state cell in blue).

Results

Electrochemical measurements

We performed preliminary electrochemical measurements in order to specify the conditions of corrosion in both configurations "severe" and "soft". Figure 2 presents the anodic linear polarization of the 310L SS in nitric acid HNO_3 8 $mol.l^{-1}$ at boiling point temperature. Based on the results obtained for a similar system [15], we qualitatively extrapolated the anodic curve below the corrosion potential E_{corr} (that is not directly measurable by electrochemistry because of the cathodic reactions) in order to visualize the

respective position of the passive and transpassive domain of the SS. Thus, we observe that in these conditions, the SS is polarized (E_{corr} ~1.11 V *vs.* SHE) in the transition of the passive to transpassive domains, where IGC is expected. In addition to vanadium(V), E_{corr} is shifted to a higher anodic potential (E_{corr} ~ 1.14 V *vs.* SHE) in the transpassive domain, where IGC is also expected. The expected corrosion currents are given in Figure 2, which shows that a higher corrosion rate is expected in presence of vanadium(V).

In conclusion, SS is polarized in both conditions in the transpassive domain, where IGC is expected. The objective of the following parts is to characterize IGC in both conditions.

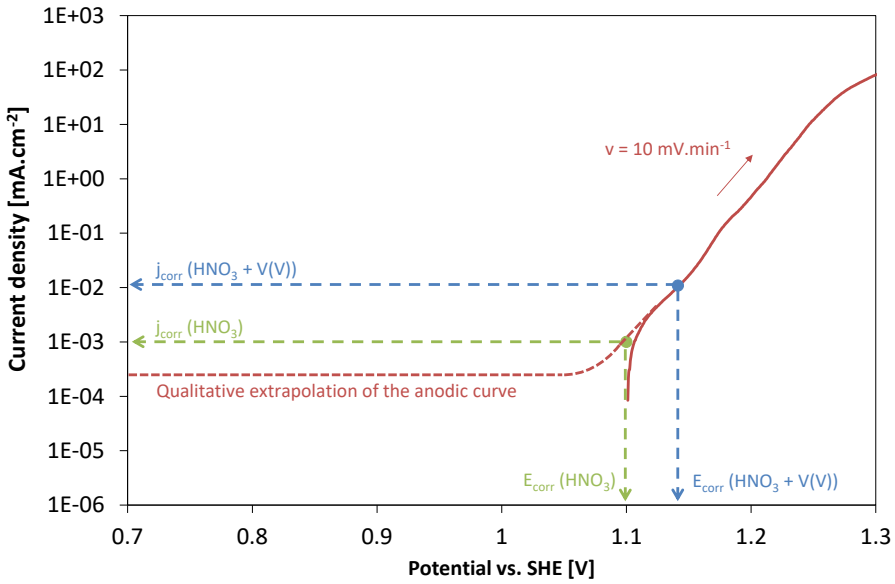

Figure 2: Anodic linear polarization curve of 310L SS in HNO_3 8 mol.l^{-1} at boiling point temperature (red continuous line). The red dashed line represents the qualitative extrapolation of the anodic curve in the passive domain. The characteristics (E_{corr} and j_{corr}) of the system are in green. Those of the system Uranus 65 in HNO_3 8 mol.l^{-1} + V(V) 150 mg.l^{-1} are in blue.

Immersion tests

In this part, we discuss the case IGC in both oxidative conditions, respectively, when the chemical medium remains the same as a function of time. The corrosion kinetics is given in terms of morphology (Figure 3 (a) for severe and Figure 5 (a) for soft conditions) and mass loss (expressed in terms of equivalent thickness loss as described in the experimental section) and corrosion rate (Figure 4 for severe and Figure 6 for soft conditions). The behavior is typical of the IGC observed for non-sensitized stainless steels and has been extensively discussed in references [15, 21, 35].

IGC begins with the creation of tight grooves at grains boundaries (80 h and 240 h in Figure 3 (a)) that progressively penetrate the steel. This leads to an increase of the SS/solution interface area, which is correlated to the corrosion rate increase as estimated by mass loss (Figure 4). This also leads to the detachment of grains that progressively affect the whole surface (2484 h in Figure 3 (a)) increasing the corrosion rate even more. When the grains detachment has affected the whole surface, the system reaches a corrosion steady state. The surface area does not evolve anymore, since the progression of grooves (increasing interface area) is counter-balanced by the grains detachment (decreasing the interface area). The phenomenology is similar for both oxidizing conditions, but the kinetics is different. It has been shown that this kind of IGC can be described by two different corrosion rates: V_{grn} and V_{ign} which correspond to corrosion rates of the grains and grains boundaries respectively. From the kinetics of IGC (Figure 4 and Figure 6), it is possible to estimate the values of V_{grn} and V_{ign}* (corresponding to the projection of V_{ign} on the vertical axis) by a semi-empirical approach presented in [35]. V_{ign} is deduced from V_{ign}* using a tortuosity factor k: $V_{ign} = V_{ign}^* \times k$, with k = 1.18 [23]. Results are given in Table 4. Both corrosion rates are faster in severe than in soft conditions. This confirms the forecasting from the electrochemical results (Figure 2).

The transient time necessary to reach the steady state can be estimated as follows [35]:

$$\frac{3}{2}\frac{D}{V_{ign}} \qquad \text{Equation 2}$$

where D represents the average grains diameter (84 µm). Therefore, the transient time is lower in severe conditions (Table 4). Durations of the experiments were fixed so that the steady state could be almost reached in both cases, that is 2564 h for severe and 16815 h for soft conditions, respectively. The objective of the following characterizations is to investigate the surface properties at steady state.

Table 4. Corrosion rates and transient time for the severe and soft IGC cases

IGC	**V_{grn} / µm.y^{-1}**	**V_{ign}* / µm.y^{-1}**	**V_{ign} / µm.y^{-1}**	**Transient time / h**
severe	273	1656	1954	565
soft	12	56	66	16703

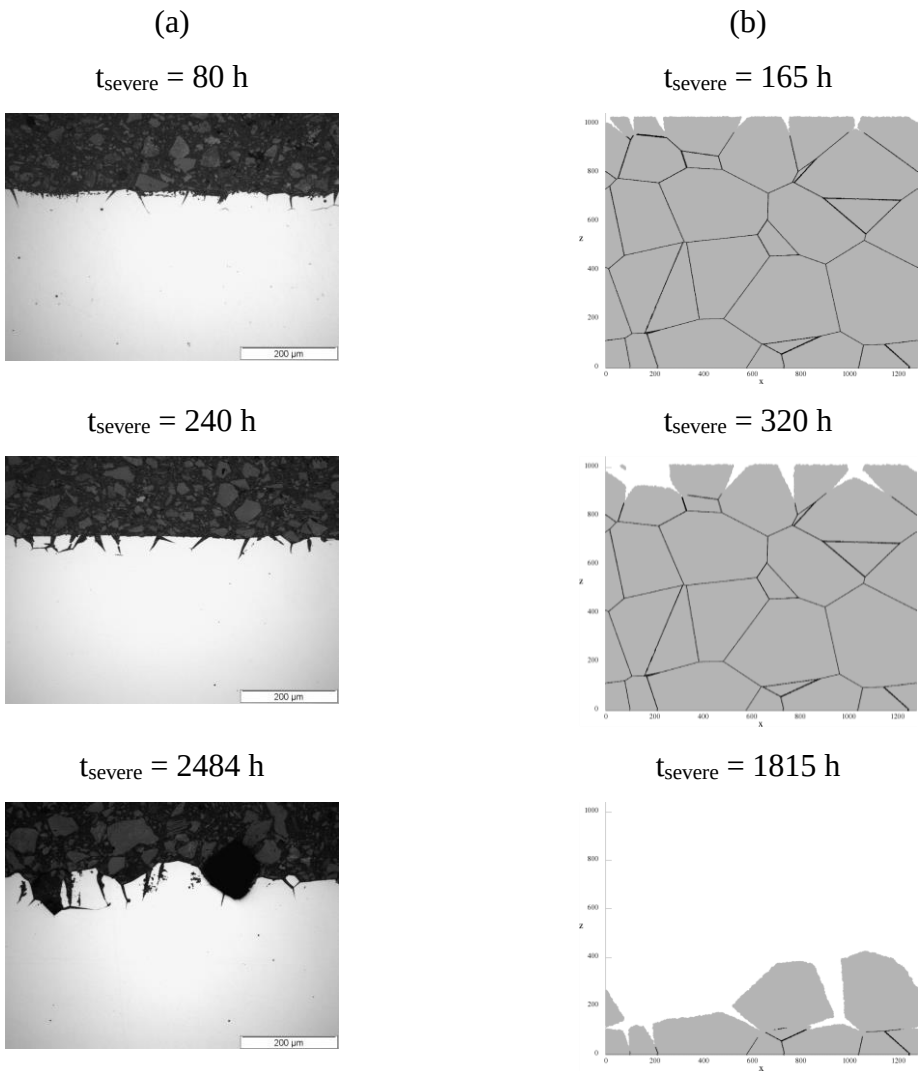

Figure 3: Evolution of the IGC observed on cross-sections in the case of a severe IGC. (a) Experiment (b) CA simulations at different times.

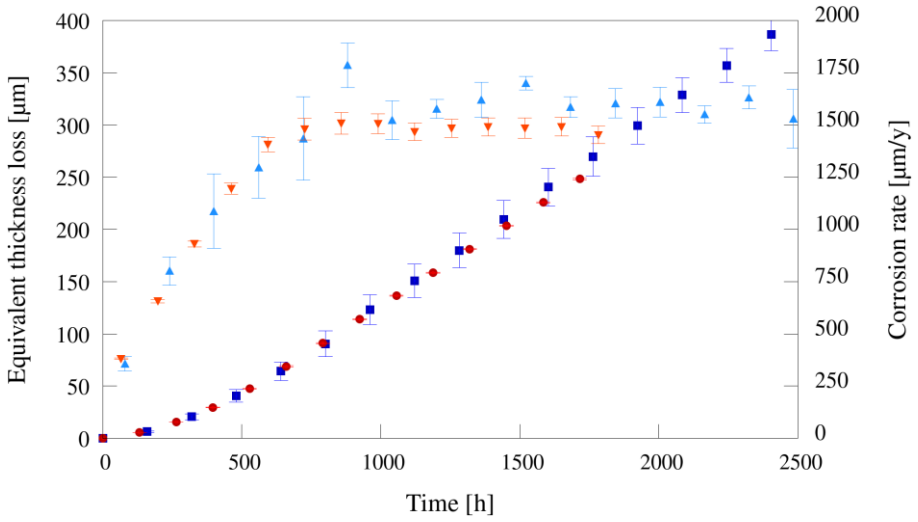

240

241 **Figure 4: Comparison between experimental results (in blue) and CA simulations (in**
242 **red) in the case of a severe IGC. Squares represent the equivalent thickness loss and**
243 **triangles the corrosion rate.**

244

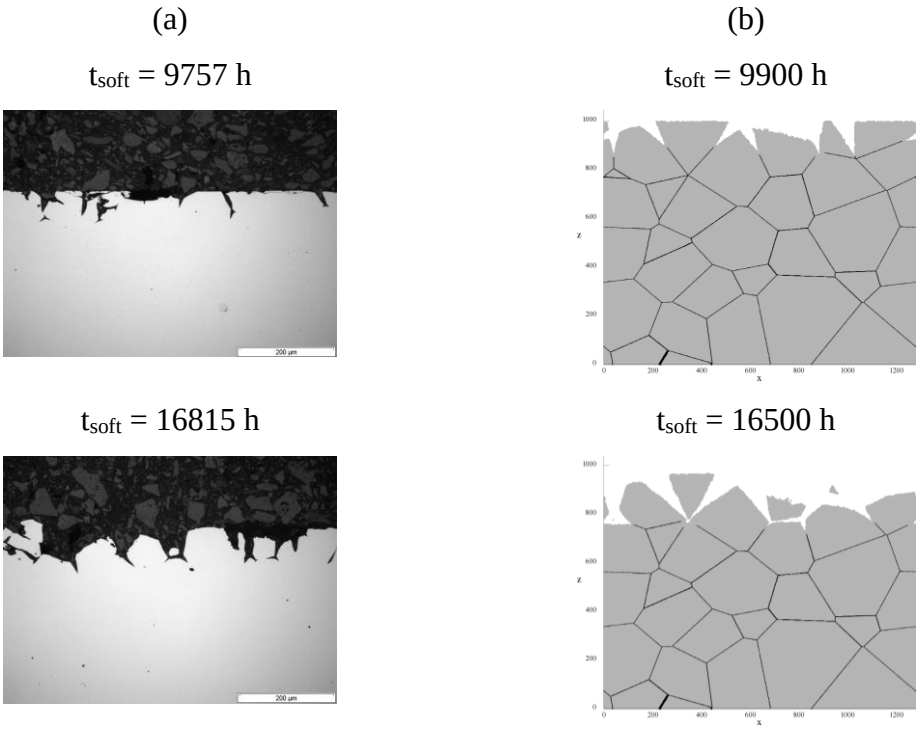

245 **Figure 5: Evolution of the IGC observed on cross-sections in the case of a soft IGC.**
246 **(a) Experiment (b) CA simulations at different times.**

247

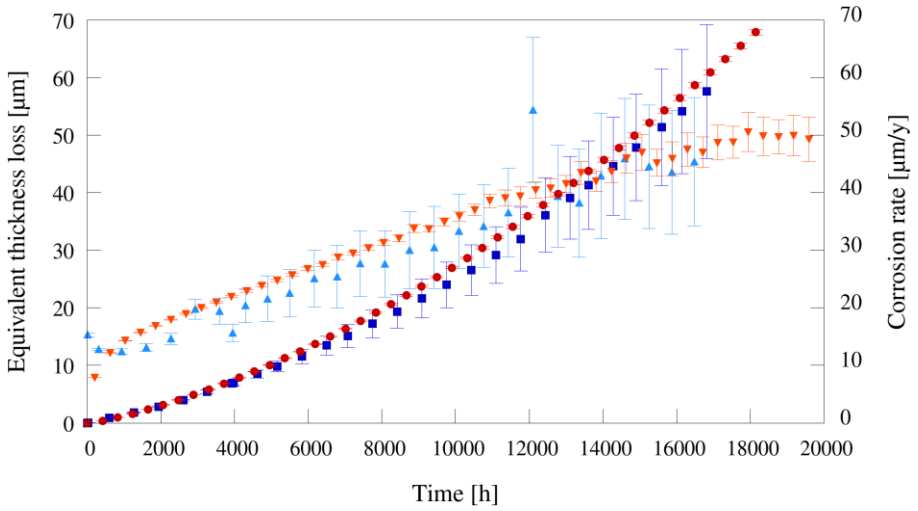

Figure 6: Comparison between experimental results (in blue) and CA simulations (in red) in the case of a soft IGC. Squares represent the equivalent thickness loss and triangles the corrosion rate.

Figure 7 presents the observation of the samples before (a) and after the corrosion tests in severe (b) and soft (c) conditions. In both conditions, samples are darker after corrosion then indicating an effect of the corrosion on the surface. Moreover, the aspect of samples is different between the severe (dark grey) and the soft (light grey). This shows that the aspect of the corroded SS is also dependent on the conditions of corrosion. The origin of the difference of aspect is further discussed in terms of chemical composition and IGC morphology of the interface.

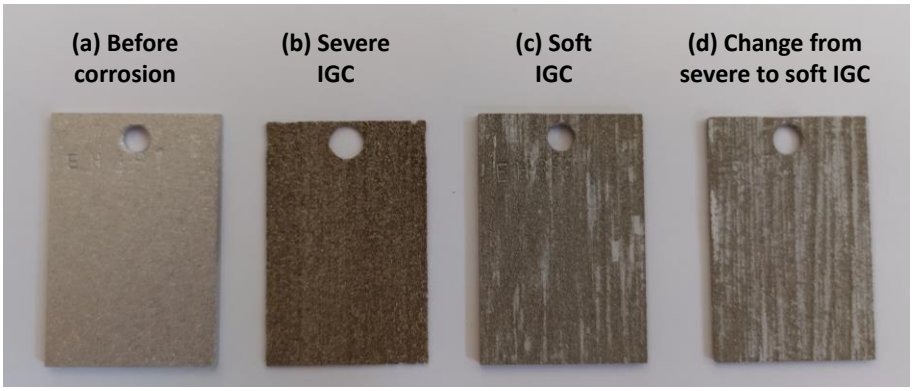

Figure 7: Aspect of the samples before (a) and after the corrosion tests in the severe (t_{severe} = 2564 h) (b), soft (t_{soft} = 16815 h) (c) and change from severe (t_{severe} = 1935 h) to soft (t_{soft} = 16815 h, *i.e.* $t_{severe+soft}$ = 17783 h) conditions (d).

Therefore, we analyzed the chemical composition of the surface using XPS relative quantification in both conditions (Figure 8). The XPS response is qualitatively similar in severe and soft conditions. The spectra show the presence of oxide and metal (associated to the presence of the metal under the oxide layer). The relative proportions of the oxide and metal contributions (for the major elements contained in the 310L SS: Iron, nickel, chromium) are reported in Figure 8 (a). The relative contribution of the oxide is larger in the severe than in the soft IGC conditions. This indicates that the oxide layer is thicker in the severe IGC conditions (with a higher corrosion potential E_{corr} as illustrated in Figure 2) than in the soft IGC conditions. This is in accordance with the results of Tcharkhtchi *et al.* who showed an increase of the oxide thickness of a 304L SS in nitric acid with the increase of the corrosion potential E_{corr} [15].

Figure 8 (b) gives the chemical composition of the oxide layer. As classically observed for these SSs corroded in nitric acid media [15, 34, 45], the oxide is mainly composed of chromium with a small proportion of iron. Nickel oxide is not observed. The severe/soft IGC conditions have a small influence on the chromium/iron ratio: a little larger relative enrichment in chromium is observed for the severe condition.

The chemical composition of the underlying metal is given in Figure 8 (c). Its relative composition differs from the bulk material: relatively enriched in nickel, compared to chromium and iron. This observation has already been reported for SSs in nitric acid [15]. It could be due to the fact that nickel is less oxidized than chromium and iron (as illustrated in Figure 8 (b)) and consequently accumulates under the oxide. This nickel enrichment seems to be larger in the severe conditions than in the soft conditions. This could be linked to the fact that the metallic zone that is analyzed by XPS is thicker (because the oxide is thinner) in soft conditions than in severe conditions. Therefore, the nickel relative enrichment in the underlying metal is more averaged with the bulk metal composition in the soft than in the severe conditions.

(a) Relative quantification of the total oxide and the underlying metal contributions (for the major elements contained in the 310L SS: Fe, Ni, Cr)

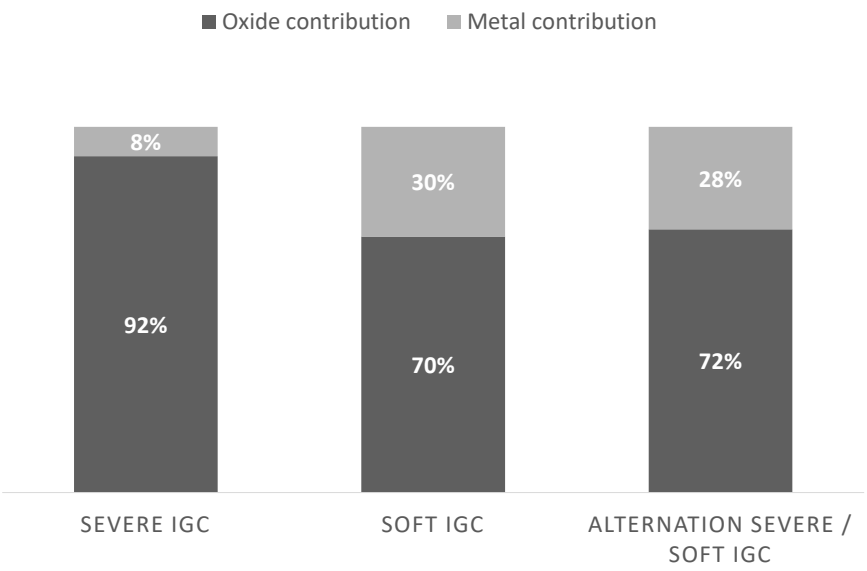

(b) Relative quantification of the composition of the oxide layer

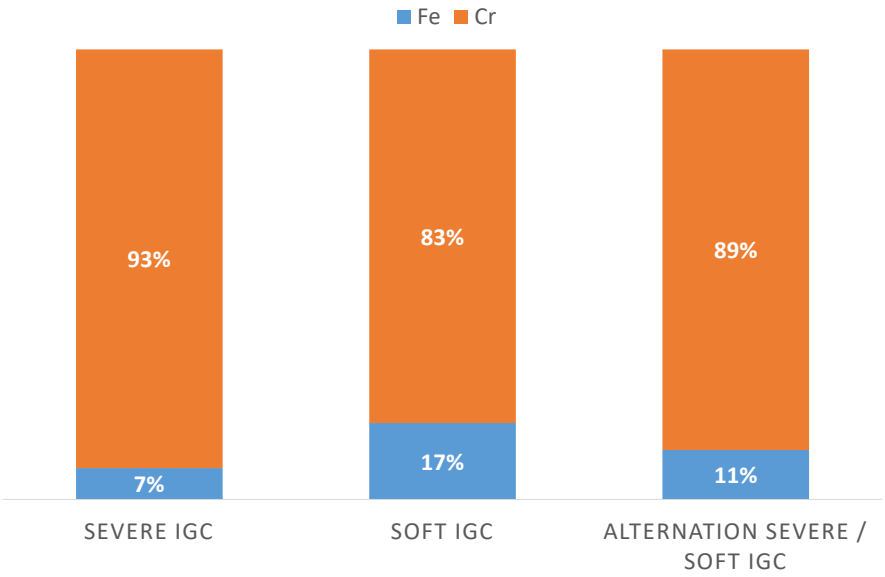

(c) Relative quantification of the composition of the underlying metal

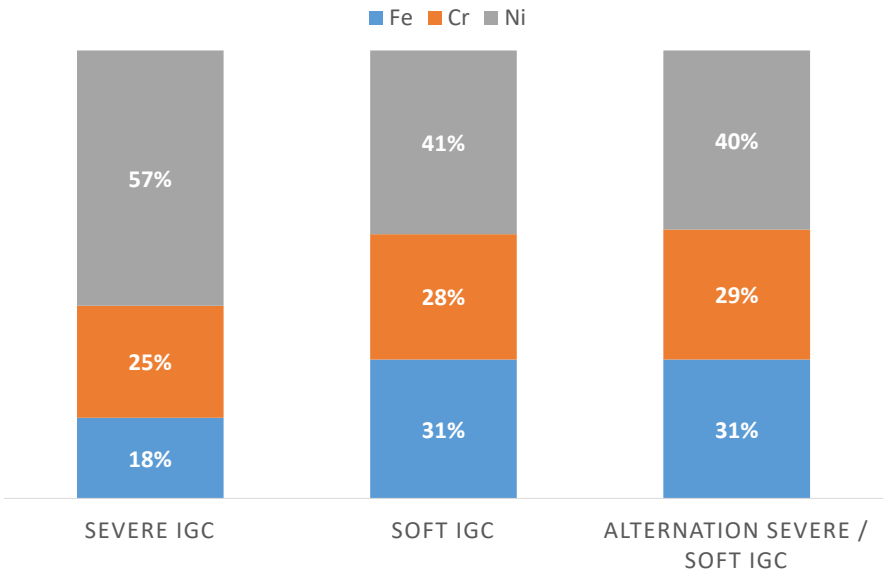

Figure 8: XPS relative quantification of the chemical characteristics of the surface of 310L SS samples corroded in the severe (t_{severe} = 2564 h), soft (t_{soft} = 16815 h) and change from severe (t_{severe} = 1935 h) to soft (t_{soft} = 16815 h, i.e. $t_{severe+soft}$ = 17783 h) conditions.

In order to get a quantitative description of the morphology, we used a CA modeling of the experiments. In a previous work [23], we showed that this model reproduces accurately the morphological evolution of IGC. This CA numerical approach enables to quantify precisely the morphological characteristics of the system, in terms of grooves angles α' distribution and the surface in contact with the solution.

The input corrosion probabilities are given in Table 5 for both IGC conditions. Moreover, conversion factors were also used in order to convert space and time scales from CA modeling to real experiments [23]: the space scaling factor A and time the scaling factor B were fixed to 0.31 μm/cell and 0.825 h/iteration, respectively. CA simulated time evolutions of the mass loss (as expressed in terms of equivalent thickness loss) are given in Figure 4 and Figure 6.

The distribution of the grooves angle α' (in degrees) at steady state of IGC is given in Figure 9. It appears that the grooves are thinner in severe (mean value 20.5, standard deviation 5.0) than in soft (mean value 26.59, standard deviation 5.9) conditions. From Beaunier [46, 47], the groove angle α is theoretically related to the V_{ign}/V_{grn} ratio by the relation:

$$\frac{V_{ign}}{V_{grn}} = \frac{1}{sin(\alpha/2)}$$ Equation 3

This theoretical value is in agreement with the one estimated by CA.

In conclusion, it appears that the more oxidant the corrosive solution, the thinner the grooves and the larger the ratio V_{ign}/V_{grn}.

SEM images of the corroded samples are given in Figure 10. It is clearly visible that there are less "small grains" that remain attached to the bulk in the severe case (a) than in soft case (b). It is due to a larger V_{ign}/V_{grn} in case (a) (Table 4), which leads to a larger grains detachment rate. From the time they are in contact with the corrosive solution, small grains are more rapidly detached from the bulk than large ones, which explains the lack of small grains on a given surface picture in the case of severe corrosion, given their shorter "life-time". As another effect of the grains life-time, it is also clearly visible in (b) and (c) that large grains that remain attached to the bulk are more deeply corroded than the small ones.

Table 5: Corrosion probabilities used as input data in the CA model and calculated from the experimental results based on the procedure given in reference [23].

	P_{ign}	P_{grn}
Severe	$P_{ign,severe} = 1$ (arbitrary maximized in order to minimize the calculation durations)	$P_{grn,severe} = P_{ign,severe} \times \frac{V_{grn,severe}}{V_{ign,severe}}$ $P_{ign,soft} = 0.140$
Soft	$P_{ign,soft} = P_{ign,severe} \times \frac{V_{ign,soft}}{V_{ign,severe}}$ $P_{ign,soft} = 0.0338$	$P_{grn,soft} = P_{ign,soft} \times \frac{V_{grn,soft}}{V_{ign,soft}}$ $P_{grn,soft} = 0.00614$

Table 6: Intergranular grooves angles α' characteristics at steady state in the different corrosion conditions (CA simulations)

Exp., time	Mean value (degrees)	Standard deviation (degrees)	Error	1/(sin(α'/2))
Severe condition t_{severe} = 825 h	20.54	5.00	0.13	5.61
Soft condition t_{soft} = 20 625 h	26.59	5.89	0.16	4.35
Change severe t_{severe} = 825 h	20.67	4.88	0.14	5.57
to soft condition $t_{severe+soft}$ = 20 625 h	26.04	5.92	0.17	4.44

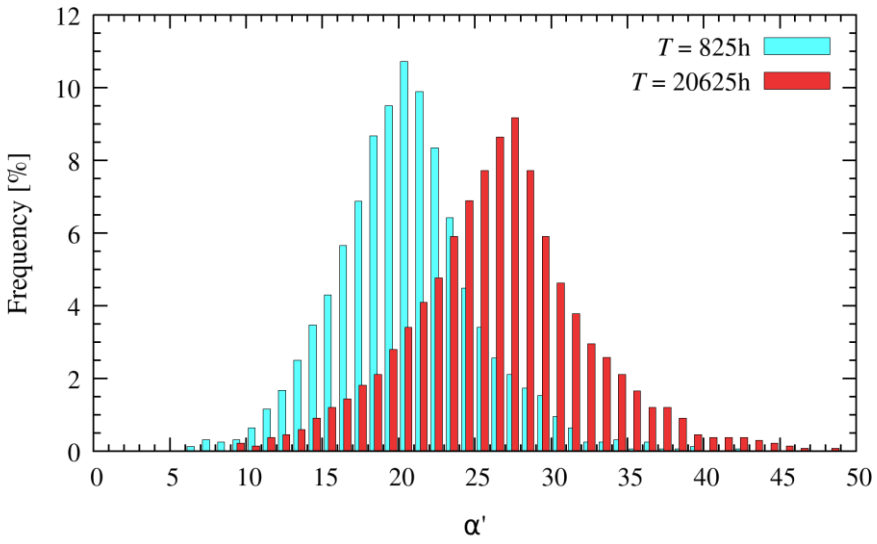

Figure 9: Distribution of the grooves angles α' in the steady state in severe (in blue, evaluated at t_{severe} = 825 h) and in soft (in red, evaluated at t_{soft} = 20625 h) conditions (CA simulations). In both cases, histograms are realized with the same classes but are slightly shifted for a better view.

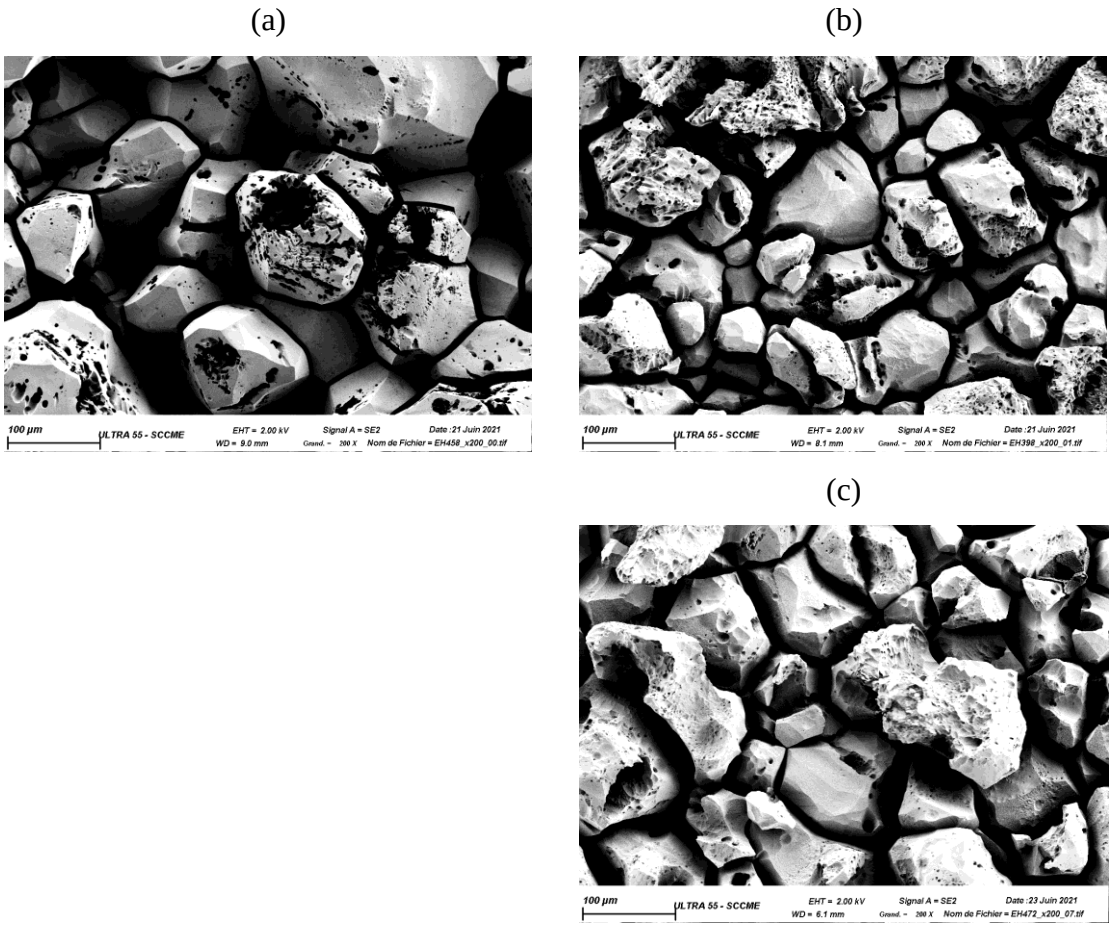

Figure 10: Observation of the samples by Scanning Electron Microscope after the corrosion tests in the severe (t_{severe} = 2564 h) (a), soft (t_{soft} = 16815 h) (b) and change from severe (t_{severe} = 1935 h) to soft (t_{soft} = 16815 h, i.e. $t_{severe+soft}$ = 17783 h) conditions (c).

Moreover, we investigated how the grooves angles distributions affect the surface in contact with the corrosive solution. For this purpose, the relative surface was determined from the CA simulations as described in the appendix 1 and 2. Results are given in Figure 11. In both severe and soft conditions, the relative surface increases from its initial "flat surface value" (100%) to reach a larger steady state value. The steady state value is higher (238.4 ± 0.4%, estimated in the interval t_{severe} = 1568 - 1732 h) for the severe conditions (therefore for the thinner grooves angle) than in soft conditions (223.7 ± 0.5%, estimated in the interval t_{soft} = 17325 - 20625 h). This is in agreement with the results of Gwinner *et al.* obtained with a model based on a 2D geometrical approach [35].

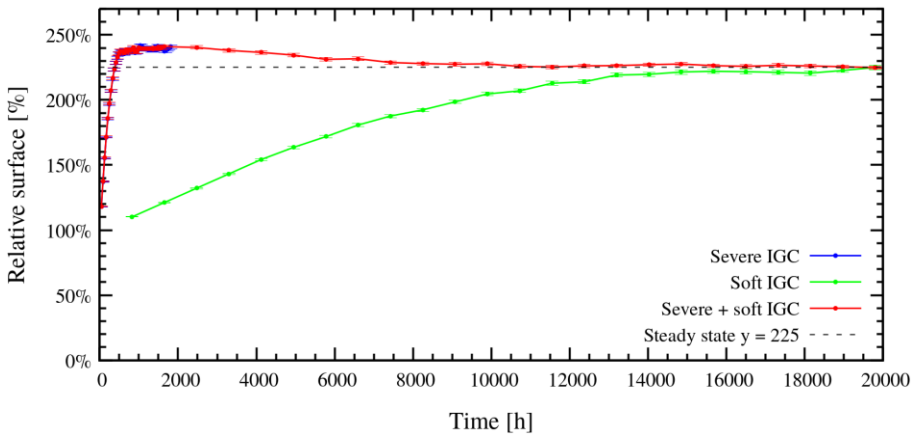

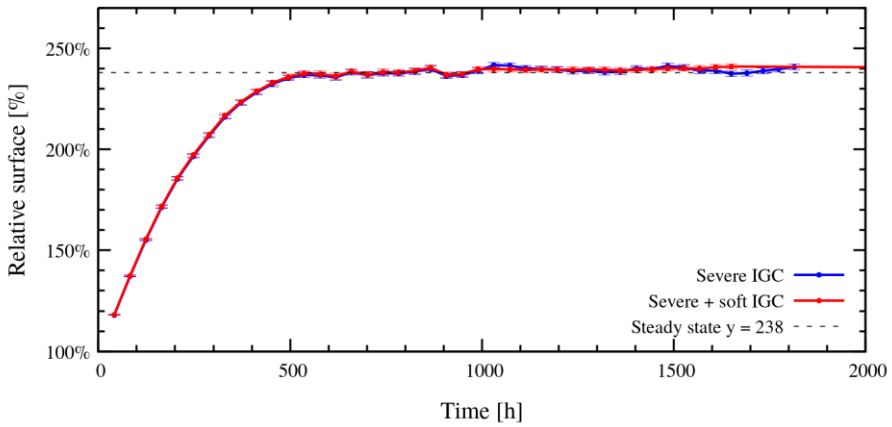

Figure 11: Relative surface for sections of the lattice for the three IGC corrosion regimes (CA simulations). The bottom plot is a zoom of the top one at short times.

We showed that in stationary conditions, the IGC characteristics depend on the oxidizing power of the corrosive medium. In more severe conditions, the SS is polarized at higher potential in the transpassive domain which has different consequences on the corrosion of the SS. Firstly, the dissolution of the SS is faster (V_{grn} is larger). This has to be related to the presence of a thicker oxide on the surface evidenced by XPS. Secondly, the intergranular corrosion is faster (V_{ign} is larger), which leads to a shorter transient time to reach the IGC steady state (in accordance with [35], where the transient time is shown to be inversely proportional to V_{ign}). Moreover, the global corrosion rate reached at steady state (which corresponds to V_{ign}*) is larger. Thirdly, the ratio V_{ign}/V_{grn} is increased which has the consequence that the grooves angles are thinner. Finally, the total surface reached at steady state is larger.

As discussed in the introduction, it is of practical interest to investigate the influence of changing the nature of the corrosive medium during the life duration. This is the objective of the following part.

Change from severe to soft IGC conditions

In order to study the effect of a change in the IGC conditions, we firstly corroded samples during 968 h in the conditions of severe IGC (with vanadium(V)) until the steady state is reached. Figure 12 and Figure 13 display the evolution of the mass and the morphology as a function of time, respectively. At the end of this early stage, the steady state is reached in terms of mass loss (Figure 12) and surface morphology (Figure 13).

Then we changed the solution into soft conditions (without vanadium(V)). The evolution of the corrosion rate is given in Figure 14 and is compared to the one in soft conditions only. The corrosion rate suddenly decreases in accordance with the new soft IGC conditions. However, it does not keep a constant value. It slowly decreases as a function of time even if the solution (that means the corrosiveness) remains the same. The system reaches a new steady state, which is identical to the previous soft IGC stationary case in terms of corrosion rate (about 50 $\mu m.y^{-1}$). Moreover, the steady state is reached at the same time in both cases. This transient time is in accordance with the one estimated by Equation 2. This corresponds to the time necessary to remove a thickness equivalent to the mean grains size. Thus, whatever the history of the SS (already corroded in severe IGC conditions or not), the corrosion needs to consume the equivalent of a layer of grains to erase the effects of this history.

Figure 13 shows the evolution of the IGC morphology from the severe conditions at steady state (at t_{severe} = 968 h) to the soft conditions (until $t_{severe+soft}$ = 17783 h). A slow evolution is observed between a highly rough surface (resulting from the severe IGC conditions) to a less rough surface (resulting from the soft IGC conditions). In the same way, SEM observations in Figure 10 show that the soft conditions tend to smooth the serious intragranular corrosion induced by severe conditions. CA simulations were performed to investigate quantitatively this point. The same input corrosion probabilities were considered as for the previous simulations (Table 5). The first step was first modeled in severe conditions during 990 h. Then the probabilities were changed into soft conditions to model the rest of the simulation.

Simulations reproduce correctly the mass loss kinetics (Figure 12) and the evolution of the morphology (Figure 13) observed experimentally. Figure 15 shows that the characteristics of the grooves angles evolve from relatively thin angles under severe conditions to larger angles in soft conditions. Consequently, the relative surface in contact with the solution decreases slowly from a value of 238.7 ± 0.7% (estimated in the interval t_{severe} = 1568 – 1733 h) in severe conditions to about 225.4 ± 0.5% (estimated in the interval $t_{severe+soft}$ = 17325 - 20625 h) in soft conditions, the same value as the experiment in steady soft conditions.

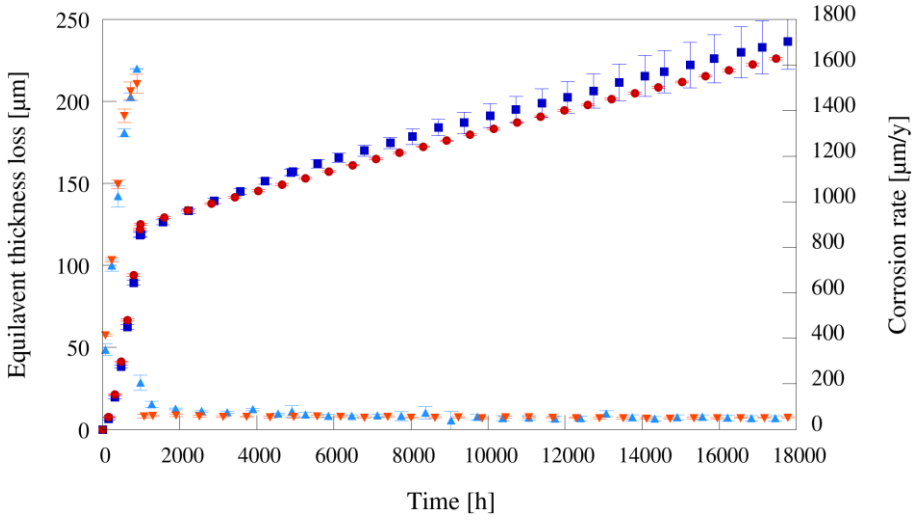

Figure 12: Comparison between experimental results (in blue) and CA simulations (in red) in the case of alternation a severe and a soft IGC. Squares represent the equivalent thickness loss and triangles the corrosion rate.

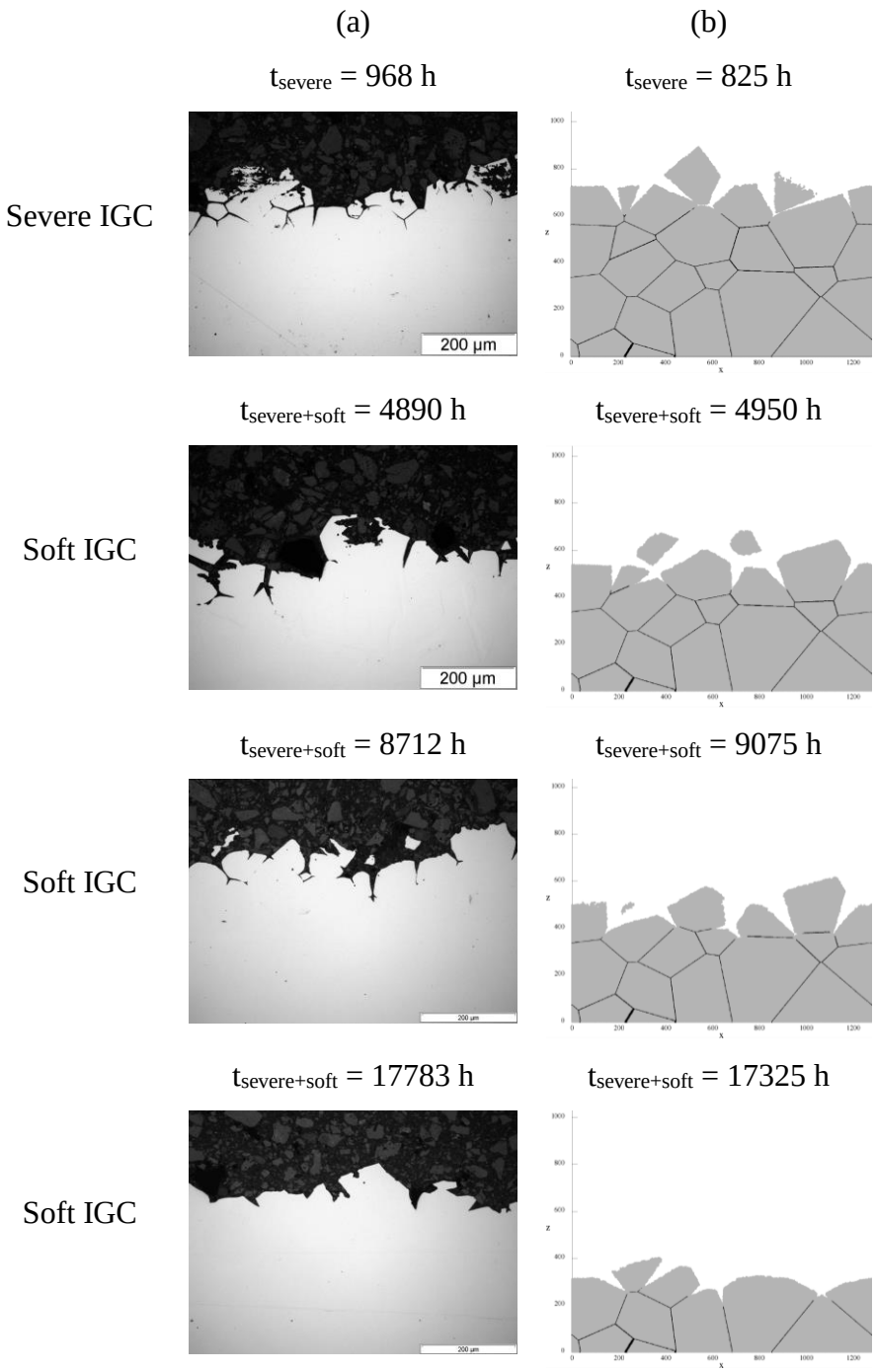

Figure 13: Evolution of the IGC observed on cross-sections in the case of alternation a severe and a soft IGC. (a) experiment and (b) CA simulations.

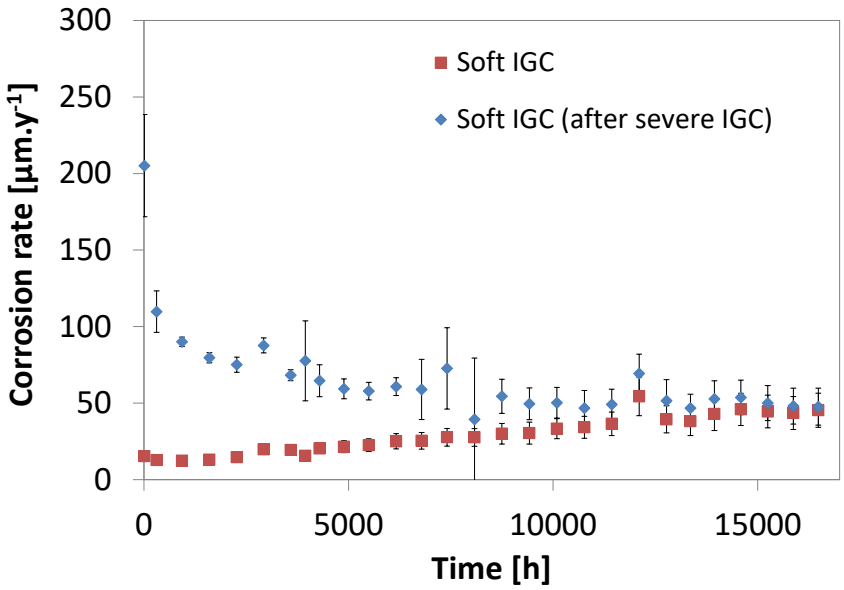

Figure 14: Comparison of the corrosion rate estimated for soft IGC only and soft IGC after severe IGC (experimental results).

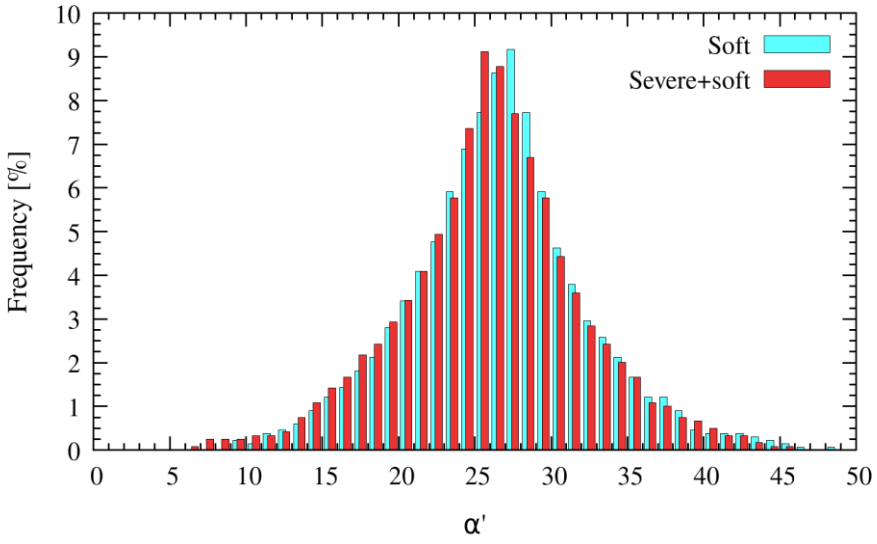

Figure 15: Distribution of the grooves angles α' in the steady state in soft (in blue, evaluated at t_{soft} = 20625 h) and in change from severe to soft (in red, evaluated at $t_{severe+soft}$ = 20625 h) conditions (CA simulations). In both cases, histograms are realized with the same classes but are slightly shifted for a better view.

The characteristics of the oxide layer on the surface also re-adapts to the new soft conditions (Figure 8). In particular, the apparent oxide thickness is similar in soft conditions and in change from severe to soft conditions (Figure 8 (a)).

Because of the oxide and morphology re-adaptation to the new soft conditions, the aspect of the surface also changes from dark grey (characteristic of the severe conditions) to light grey (characteristic of the soft conditions) as shown in Figure 7.

Conclusions

We first investigated the impact of the oxidizing character of the nitric medium on the evolution of the IGC of an austenitic SS. In two different stationary chemical conditions (severe and soft, respectively), we showed that the SS reaches a different steady state in terms of the oxide and the geometrical natures of the interface: the oxide is thicker, the intergranular grooves are thinner and the surface area is larger with the oxidizing character of the nitric medium. Then we investigated the effect of an alternative “severe then soft” corrosion sequence. We showed that the system re-adapted to the soft conditions after a certain duration (which corresponds to the time necessary to corrode a thickness equivalent to the mean grains size of the SS) without memory effect from the previous severe ones: the corrosion rate, the geometrical nature of the interface and the thickness of the oxide become similar to the system corroded in soft conditions only. In other words, whatever the IGC history of a SS, the new conditions of IGC corrosion need to consume the equivalent of a layer of grains to erase the effects of this history.

Acknowledgments

The authors thank Orano for financial support. They thank also R. Golchha for his careful proofreading. D. di Caprio would like to thank Dr. B. Diawara for fruitful discussions and introducing him to the marching cubes algorithm.

Appendix

Appendix 1: solid/solution frontier estimation, marching square type algorithm

In this section, we detail the algorithm used to measure the length of the border line between the solution cells and the solid corresponding to GRN or IGN cells. For 3D objects, the marching cubes algorithm [48] is often used to determine contour lines. Given its simplicity, the algorithm finds applications in video games but also in medicine, for 3D visualization of volume data from magnetic resonance imaging and computed tomography scans [48, 49]. In the case of 2D images, the algorithm is referred to as marching squares. In the context of this paper, the algorithm is further adapted for a 2D grid based on rectangles paving the plane instead of squares. The details about the system coordinates used for the hexagonal lattice are given hereafter.

The hexagonal lattice

The plane of the hexagonal lattice structure is the horizontal 0xy plane, with, for z = 0, the first line y = 0, points starting at x = 0:5 and placed in the Ox direction at a distance of 1 as shown in Figure 16 in blue points.

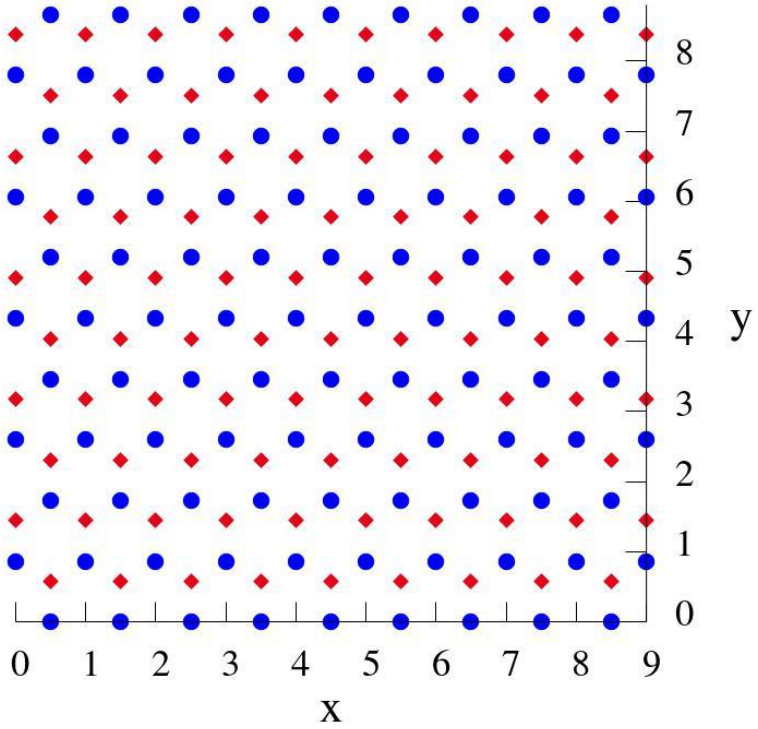

Figure 16: Horizontal sections of the hexagonal lattice. Two consecutive planes, z = 0 and z = $(2/3)^{1/2}$, are shown with respectively blue and red points.

Once these first two planes are defined, the rest of the lattice is derived. In particular, in the experiments and in the simulations vertical sections are studied. The layout of points in the vertical sections for the simulation is shown in Figure 17 where we have considered vertical Oxz planes with constant y coordinate.

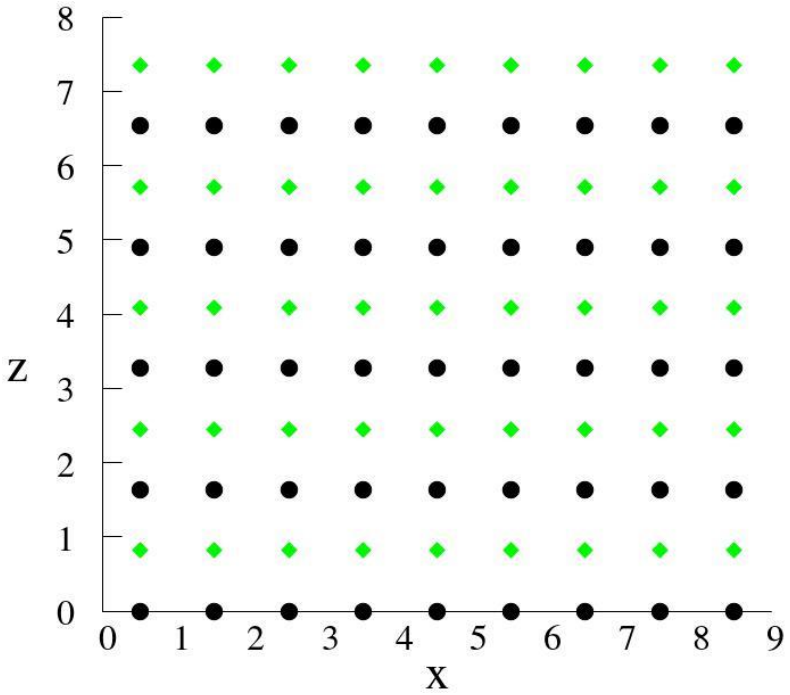

Figure 17: Vertical sections of the lattice. Two consecutive planes for y = 0 and y = $(3)^{1/2}/2$ are shown with respectively black and green points.

From the figure, it is clear that we have rectangles paving the plane.

The marching rectangles algorithm

Then, the algorithm consists in summing the contributions to the solution/solid border coming from each rectangle in the plane. For this aim, we first list all possible contributions coming from the configurations as shown in Figure 18. By assigning "1" to an intergranular or granular point and "0" to a solution point and starting from the bottom left corner, in an anticlockwise order, we obtain a binary number which is assigned to the corresponding case.

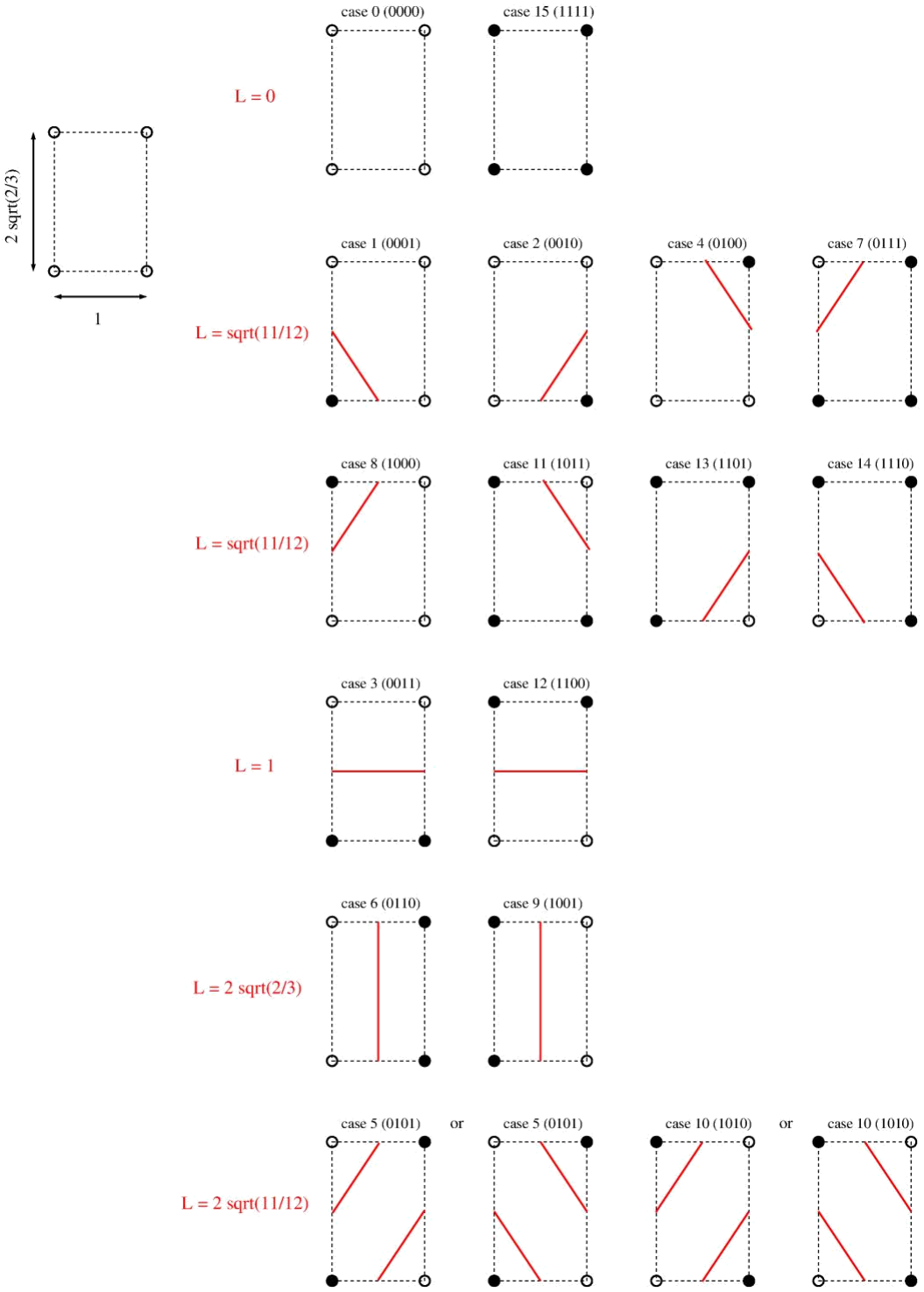

Figure 18: On the top left the elementary rectangle and its dimensions. On the right are listed the length contributions and the corresponding layout of the points. Empty circles are for solution points and black points are for solid granular or intergranular cells.

The cases in the first line correspond to cases inside the solution or inside the solid and they naturally do not contribute to the border length: L = 0. The cases in the last line

correspond to a saddle point situation where we have two lines but for which the line orientation can be ambiguous. However, the contribution to the border length is the same for both orientations so that the result is unchanged despite the ambiguity. Other border lengths correspond to their geometrical contribution. All rectangles constituting the lattice are computed and their contribution is summed up which gives the final estimation of the border length. The ratio of this length divided by the straight lateral length of the system is what we consider to be the relative surface, which is in fact a line for the 2D sections.

Appendix 2: extracting the grain scale relative surface

Simulated sections of the system in Figure 3, Figure 5 and Figure 13 clearly show that we have two types of relative surface contributions. One with short length scale variations corresponding to the dissolution of a single grain and one at a larger scale, the scale of grains, due to IGC and detachment of grains. It is this last contribution that we are interested in. However, the algorithm presented above does not distinguish the two, as it provides the total separation line between solid and solution.

We present, hereafter, the method used to separate the contribution from IGC and grain detachment from the contribution at a short length scale due to dissolution. For this aim, we perform supplementary simulations for the dissolution of an exclusively granular material with an initial plane surface and in the identical conditions of severe, soft and variable IGC conditions as for the IGC material model. Results are obtained averaging over 2000 sections. Figure 19 shows the relative surface, roughness for the three cases.

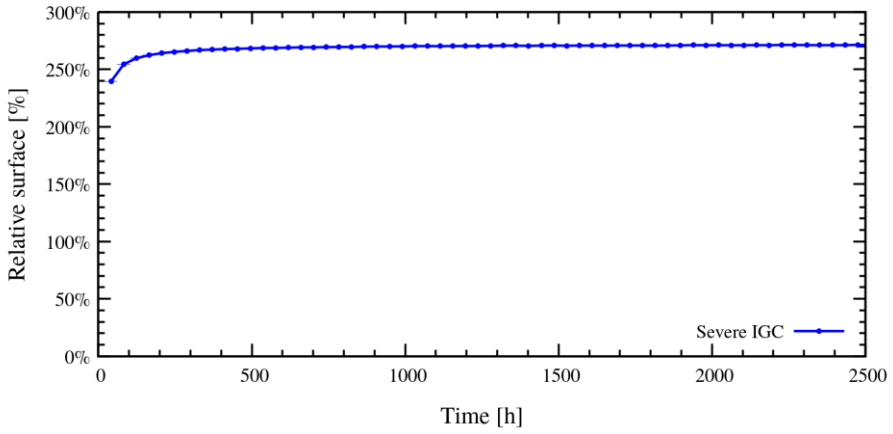

534

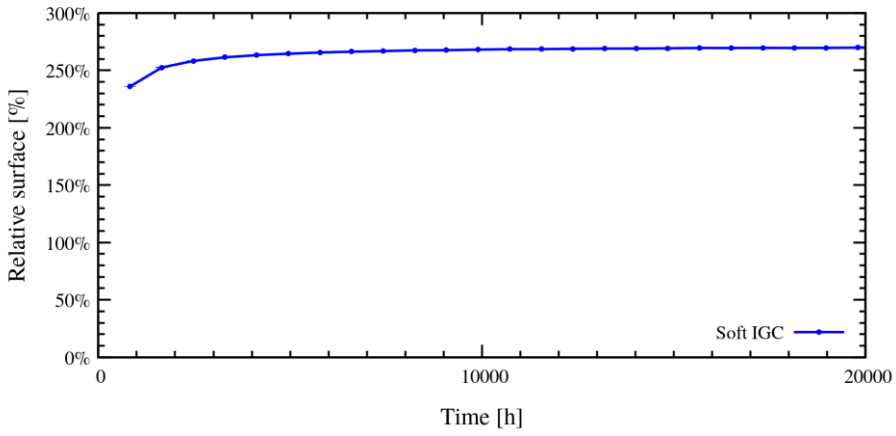

535

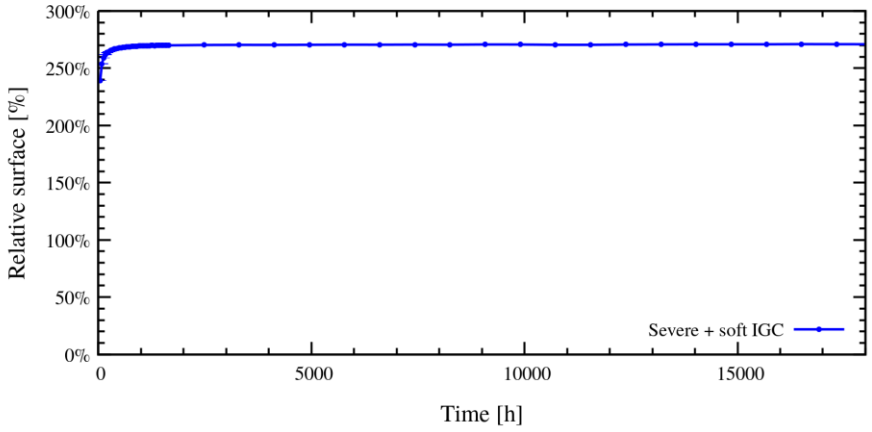

536

537 **Figure 19: Solid/solution relative interface for successively the severe, soft and**
538 **variable IGC conditions for granular dissolution.**

539

540 The relative surface varies with time: it increases before reaching a steady state. This is
541 why we use this time dependent quantity to renormalize the relative surface and not the
542 steady state value. Thus the relative surface corresponding to IGC and grain detachment is
543 obtained from the relative surface obtained by the algorithm by dividing it by the relative
544 surface for exclusively granular dissolution. The procedure has been tested by applying it

to the study presented in [23], and the results compare well within the error bars. The results in the case of the present paper study are presented in Figure 11. Averages are performed using 100 Voronoï structures with for each 9 sections, this ensures that sections are sufficiently spaced to avoid undesirable correlations.

References

1. Bal, K.S., J.D. Majumdar, and A.R. Choudhury, *Study of intergranular corrosion mechanism of fiber laser welded 3-mm-thick Hastelloy C-276 sheet.* Corrosion Science, 2019. **157**: p. 406-419.
2. Kaithwas, C.K., et al., *'Hall-Petch' type of relationship between the extent of intergranular corrosion and grain size in a Ni-based superalloy.* Corrosion Science, 2020. **175**.
3. Zhang, J.Y., et al., *New perspectives on the grain boundary misorientation angle dependent intergranular corrosion of polycrystalline nickel-based 625 alloy.* Corrosion Science, 2020. **172**.
4. de Bonfils-Lahovary, M.L., et al., *Influence of hydrogen on the propagation of intergranular corrosion defects in 2024 aluminium alloy.* Corrosion Science, 2019. **148**: p. 198-205.
5. Kairy, S.K., et al., *The role of microstructure and microchemistry on intergranular corrosion of aluminium alloy AA7085-T7452.* Corrosion Science, 2018. **143**: p. 414-427.
6. Zhang, X.X., et al., *Intergranular corrosion in AA2024-T3 aluminium alloy: The influence of stored energy and prediction.* Corrosion Science, 2019. **155**: p. 1-12.
7. Hu, S., et al., *Intergranular corrosion behavior of low-chromium ferritic stainless steel without Cr-carbide precipitation after aging.* Corrosion Science, 2020. **166**.
8. Morshed-Behbahani, K., et al., *An electrochemical study on the effect of stabilization and sensitization heat treatments on the intergranular corrosion behaviour of AISI 321H austenitic stainless steel.* Corrosion Science, 2018. **138**: p. 28-41.
9. Pradhan, S.K., P. Bhuyan, and S. Mandal, *Individual and synergistic influences of microstructural features on intergranular corrosion behavior in extra-low carbon type 304L austenitic stainless steel.* Corrosion Science, 2018. **139**: p. 319-332.
10. Fauvet, P., *Corrosion issues in nuclear fuel reprocessing plants*, in *Nuclear corrosion science and engineering*, D. Feron, Editor. 2012, Woodhead Publishing. p. 679-728.
11. Fauvet, P., et al., *Corrosion mechanisms of austenitic stainless steels in nitric media used in reprocessing plants.* Journal of Nuclear Materials, 2008. **375**(1): p. 52.
12. Kato, C., *Corrosion in Nuclear Fuel Reprocessing Plants: Corrosion in Boiling Nitric Acid*, in *Comprehensive Nuclear Material book*. 2020, Elsevier.
13. Emery, A., *Corrosion intergranulaire des aciers inoxydables austénitiques en milieu acide nitrique oxydant*. 2019, Université PSL.
14. Komatsu, A., et al., *Effect of local segregation of phosphorous on intergranular corrosion of type 310 stainless steel in boiling nitric acid.* Zairyo to Kankyo, 2014. **63**(3): p. 98-103.

15. Tcharkhtchi-Gillard, E., et al., *Kinetics of the oxidation of stainless steel in hot and concentrated nitric acid in the passive and transpassive domains.* Corrosion Science, 2016. **107**: p. 182-192.
16. Ueno, F., et al. *Intergranular corrosion mechanism of ultra-low carbon type 304 stainless steel in a nuclear reprocessing plant*. in *Global 2007*. 2007. Boise, Idaho.
17. Ueno, F., et al., *Corrosion phenomenon of stainless steel in boiling nitric acid solution using large-scale mock-up of reduced pressurized evaporator.* Journal of Nuclear Science and Technology, 2008. **45**(10): p. 1091-1097.
18. Ueno, F., et al. *Study on the effect of phosphorous concentration on intergranular corrosion of stainless steel in boiling nitric acid solution*. in *Eurocorr*. 2014. Pise (Italie).
19. Whillock, G.O.H. and B.F. Dunnett. *Intergranular corrosion testing of austenitic stainless steels in nitric acid solutions*. in *Eurocorr 2004*. 2004. Nice (France): Société de Chimie Industrielle, Paris (France). INIS-FR-3830.
20. Whillock, G.O.H., B.F. Dunnett, and M. Takeuchi, *Techniques for measuring the end-grain corrosion resistance of austenitic stainless steels.* Corrosion, 2005. **61**(1): p. 58-67.
21. Bague, V., et al., *Determination of the long-term intergranular corrosion rate of stainless steel in concentrated nitric acid.* Journal of Nuclear Materials, 2009. **392**(3): p. 396-404.
22. Jothilakshmi, N., P.P. Nanekar, and V. Kain, *Assessment of Intergranular Corrosion Attack in Austenitic Stainless Steel Using Ultrasonic Measurements.* Corrosion, 2013. **69**(4): p. 388-395.
23. Guiso, S., et al., *Intergranular corrosion: Comparison between experiments and cellular automata.* Corrosion Science, 2020. **177**: p. 108953.
24. Gwinner, B., et al., *A stereological approach for measuring the groove angles of intergranular corrosion.* Corrosion Science, 2017. **115**: p. 1-7.
25. Ioka, I., et al. *Susceptibility of intergranular corrosion for extra high purity austenitic stainless steel in nitric acid*. in *Proceedings of 16th International Conference on Nuclear Engineering, ICONE-16*. 2008.
26. Motooka, T., C. Kato, and M. Yamamoto, *Effect of Reoxidation Rate of Chromium and Vanadium Ions on Corrosion Rate of Stainless Steel in Boiling Nitric Acid Solutions.* Corrosion Engineering, 2010. **59**(1): p. 12-20.
27. Motooka, T. and M. Yamamoto, *Corrosion behavior of stainless steel in nitric acid solutions including neptunium.* Zairyo to Kankyo 2008. **57**(12): p. 536-541.
28. Ningshen, S., et al., *Corrosion assessment of nitric acid grade austenitic stainless steels.* Corrosion Science, 2009. **51**(2): p. 322-329.
29. Takeuchi, M. and G.O.H. Whillock, *Effect of Endgrain Attack on Corrosion of 18Cr–10Ni Austenitic Stainless Steel*
in Simulated Dissolver Liquor. Journal of NUCLEAR SCIENCE and TECHNOLOGY, 2004. **41**(6): p. 702-708.
30. Wang, W., et al., *Influence of grain size on susceptibility of Cr-Ni austenitic stainless steel to intergranular attack in nitric acid.* Journal of Iron and Steel Research, 2010. **22**(1).
31. Ioka, I., et al., *Correlation between intergranular corrosion and impurities of extra high purity austenitic stainless steels.* Journal of Power and Energy Systems, 2010. **4**(1): p. 105-112.
32. Guiso, S., et al., *Intergranular corrosion: Comparison between experiments and cellular automata.* Corrosion Science, 2020. **177**.

33. Ningshen, S. and M. Sakairi, *Corrosion degradation of AISI type 304L stainless steel for application in nuclear reprocessing plant.* Journal of Solid State Electrochemistry, 2015. **19**(12): p. 3533-3542.
34. Robin, R., F. Miserque, and V. Spagnol, *Correlation between composition of passive layer and corrosion behavior of high Si-containing austenitic stainless steels in nitric acid.* Journal of Nuclear Materials, 2008. **375**(1): p. 65-71.
35. Gwinner, B., et al., *Towards a reliable determination of the intergranular corrosion rate of austenitic stainless steel in oxidizing media.* Corrosion Science, 2016. **107**: p. 60-75.
36. Igarashi, T., et al. *Intergranular Corrosion Simulation of Stainless Steel Considering Nitric Acid Solution Condition*. in *Eurocorr*. 2016.
37. Igarashi, T., et al. *Three dimensional computational modelling and simulation of intergranular corrosion propagation of stainless steel*. in *19th International Corrosion Congress*. 2014. Jeju, Korea.
38. Guiso, S., et al., *Influence of the grid cell geometry on 3D cellular automata behavior in intergranular corrosion.* Journal of Computational Science, 2021. **53**: p. 101322.
39. Bhise, S. and V. Kain, *Methodology based on potential measurement for predicting corrosion behaviour of SS 304L in boiling nitric acid containing oxidising ions.* Corrosion Engineering, Science and Technology, 2012. **47**(1).
40. Ghiban, B., et al., *Austenitic stainless steels corrosion properties modified by silicon alloying.* Metalurgia International, 2008. **13**(7): p. 39-42.
41. Kain, V., et al., *Corrosion of non-sensitized austenitic stainless steels in nitric acid environment: an electrochemical approach.* Advanced Materials Research (Durnten-Zurich, Switzerland), 2013. **794**: p. 517-529.
42. Pourbaix, M., *Atlas d'équilibres électrochimiques à 25°C*. 1963, Paris: Gauthier-Villars & Cie.
43. Grosvenor, A.P., et al., *Investigation of multiplet splitting of Fe 2p XPS spectra and bonding in iron compounds.* SURFACE AND INTERFACE ANALYSIS, 2004. **36**(12): p. 1564-1574.
44. Marchetti, L., et al., *XPS study of Ni-base alloys oxide films formed in primary conditions of pressurized water reactor.* SURFACE AND INTERFACE ANALYSIS, 2015. **47**(5): p. 632-642.
45. Laurent, B., et al., *Dissolution and Passivation of a Silicon-Rich Austenitic Stainless Steel during Active-Passive Cycles in Sulfuric and Nitric Acid.* Journal of The Electrochemical Society, 2017. **164**(13): p. C892-C900.
46. Beaunier, L., *Corrosion of grain boundaries : initiation processes and testing.* Journal de Physique, 1982. **Colloque C6, supplement to Journal de Physique n° 12**(Tome 43): p. C6-271 – C6-282.
47. Beaunier, L., M. Froment, and C. Vignaud, *A kinetical model for the electrochemical grooving of grain boundaries.* Electrochimica Acta, 1980. **25**(10): p. 1239-1246.
48. Lorensen, W.E. and H.E. Cline, *Marching cubes: a high resolution 3D surface construction algorithm*, in *Seminal graphics: pioneering efforts that shaped the field*. 1998, Association for Computing Machinery. p. 347–353.
49. Zhang, Y.J., *Geometric Modeling and Mesh Generation from Scanned Images*. 2018, Chapman and Hall/CRC. p. 145-149.